Journal of Applied Physics

Quantitative photothermal lock-in thermography imaging of curved surfaces of cylindrical solids

Cite as: J. Appl. Phys. **127**, 195101 (2020); https://doi.org/10.1063/5.0007779
Submitted: 18 March 2020 . Accepted: 28 April 2020 . Published Online: 15 May 2020

Yu Liu, Ti Sun, Chinhua Wang, and Andreas Mandelis

Journal of Applied Physics ARTICLE scitation.org/journal/jap

Quantitative photothermal lock-in thermography imaging of curved surfaces of cylindrical solids

Cite as: J. Appl. Phys. **127**, 195101 (2020); doi: 10.1063/5.0007779
Submitted: 18 March 2020 · Accepted: 28 April 2020 ·
Published Online: 15 May 2020

Yu Liu,[1,2] Ti Sun,[1,2] Chinhua Wang,[1,2,a)] and Andreas Mandelis[3]

AFFILIATIONS

[1]School of Optoelectronics Science and Engineering and Collaborative Innovation Center of Suzhou Nano Science and Technology, Soochow University, Suzhou, Jiangsu 215006, People's Republic of China
[2]Key Lab of Advanced Optical Manufacturing Technologies of Jiangsu Province and Key Lab of Modern Optical Technologies of Education Ministry of China, Suzhou, Jiangsu 215006, People's Republic of China
[3]Department of Mechanical and Industrial Engineering, Center for Advanced Diffusion-Wave and Photoacoustic Technologies (CADIPT), University of Toronto, Toronto M5S 3G8, Ontario, Canada

Note: This paper is part of the Special Topic on Photothermics.
a)Author to whom correspondence should be addressed: chinhua.wang@suda.edu.cn

ABSTRACT

We extend the applications of photothermal radiometric diagnostics to continuously curved cylindrical surface solids using lock-in thermography (LIT) imaging, in which both the photothermally induced surface temperature and the angularly dependent infrared radiation emitted by the curved surface are not constant. Specifically, a theoretical photothermal model is established based on the Green Function method from which the thermal-wave field distribution at different azimuthal angles on the curved surface is obtained and characteristics of the thermal-wave field with different material and measurement parameters/schemes are discussed. A laser-infrared photothermal lock-in imaging system for solid cylindrical samples is established, and the thermal diffusivity of AISI 304 cylindrical steel samples is measured directly based on the LIT images combined with empirically obtained infrared radiation angular distributions over the curved surfaces. The experimental results are in excellent agreement with the theory, which provides a fast and non-destructive quantitative tool for thermophysical evaluation of curved surface solids.

I. INTRODUCTION

Since the photothermal radiometry (PTR) technique was introduced by Nordal and Kanstad[1–3] in the early 1980s, it has become a powerful tool for the thermophysical characterization and the non-destructive evaluation of broad classes of materials[4–7] due to its non-contact, non-destructive, and highly sensitive nature. The basic principle of PTR is the analysis of the thermal waves generated in a material and thus the infrared radiation emitted from the material surface as a consequence of the absorption of an intensity-modulated light beam. Differences in infrared radiation are detected due to different thermal responses to the modulated incident excitation, containing information on thermophysical and structural (internal and surface) properties of materials. Conventional PTR uses either pulsed[7,8] or periodically modulated[9,10] thermal excitation and collects infrared radiation from a single point on the sample, which is subsequently detected with either time-resolved or frequency-domain lock-in measurements. In order to obtain a photothermal image of the material of interest, point-by-point scanning of the relative position of the excitation source (e.g., a laser) on a sample under test must be implemented.[11,12] However, the amount of time required for coordinate scanning is usually long, especially for large structures when aiming at imaging deep subsurface regions, a fact that practically limits this application. In the 1990s, Busse *et al.* introduced lock-in thermography (LIT), an infrared camera based photothermal imaging technique which greatly improves the image contrast, signal-to-noise ratio (SNR), and more importantly, the speed of sample characterization.[13,14] The basic principle of the technique is the optically induced thermal wave generation simultaneously on the whole sample surface and sequential monitoring of all pixels using both thermographic and lock-in techniques, which

combines advantages of both conventional thermal wave measurement and thermography using a commercial IR camera. LIT and its optoelectronic counterpart, lock-in carrierography (LIC), have shown their advantages with important applications having been reported in diverse fields of non-destructive evaluation.[15–19] However, most of the aforementioned applications are limited to flat or near-flat samples and the use of one-dimensional planar photothermal models so as to exclude the complicating effect of non-planar sample geometries on the thermal-wave field in addition to the effects of the thermophysical properties on the signal.

With the growth of PTR and LIT applications, the requirement for non-planar geometry measurements of thermophysical properties and non-destructive evaluation has also been proposed and investigated. Cylindrical[20–25] and spherical[26–29] PTR models in the frequency domain for either uniform or composite structures have been proposed and validated using either the Green function[20–23,26–28,30–31] or the thermal quadrupole method.[24–25,29] All those investigations show that the PTR signal is a sensitive function not only of thermophysical properties, but also of the surface curvature. Using the Green function method, a solid-wedge sample was also characterized with the frequency scanned PTR at a selected single coordinate location.[32] Yet, quantitative LIT imaging of non-planar geometries is still rare to-date. Very recently, Wang *et al.* reported a theoretical and experimental LIT imaging investigation of an angled corner structure with an arbitrary opening angle irradiated with a periodically modulated and collimated laser beam based on the Green function method.[33] The angled corner structure was formed by two flat surfaces with an intersecting angle so that the LIT image was actually obtained from two flat surfaces rather than a continuous curved surface. In this work, we report a theoretical and experimental imaging investigation of cylindrical curved samples using LIT in which both the photothermally induced surface temperature and the angularly dependent infrared radiation of the continuously curved surface are not constant over the imaged area. Experimental LIT results of AISI 304 cylindrical steel rods showed excellent agreement with the theory in that both the coordinate sensitive thermal-wave field and the coordinate-dependent infrared radiation of the curved surface can be very well predicted by the theory when normalized by the empirically determined combined instrumental and cylindrical angular distribution function of emitted infrared radiation from the surface.

II. THERMAL-WAVE FIELD OF A CURVED CYLINDRICAL STRUCTURE

The geometry and coordinates of the LIT measurement of a cylindrical sample are shown in Fig. 1. The curved surface of the cylindrical solid is uniformly irradiated by a collimated laser beam with a modulation frequency f. The width of the collimated beam is subtended by angle θ_0. The harmonic thermal-wave equation for the cylinder can be written as

$$\nabla^2 T(\vec{r},\omega) - \sigma^2(\omega) T(\vec{r},\omega) = -\frac{1}{k} Q(\vec{r},\omega), \tag{1}$$

where $\sigma\sigma(\omega) = (i\omega/\alpha)^{1/2} = (1+i)\sqrt{\omega/2\alpha}$ is the complex thermal wave-number, α (m^2/s) and k (W/m K) are, respectively, the thermal diffusivity and thermal conductivity of the material, $\omega = 2\pi f$ is the angular modulation frequency of the laser beam, f (Hz) is the modulation frequency of the incident illumination, and $Q(\vec{r},\omega)$ is the volume thermal source in the material at coordinates $\vec{r} = (r, \varphi)$. Based on the Green function method, the general solution for Eq. (1) can be expressed as[30]

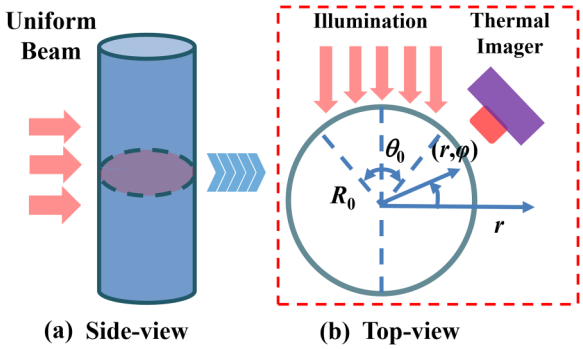

FIG. 1. Geometry and coordinates of laser-beam-irradiated cylindrical solid and detection imager. (a) Side view and (b) top view.

$$T(\vec{r},\omega) = \left(\frac{\alpha}{k}\right) \iiint_{V_0} Q(\vec{r}_0,\omega) G(\vec{r}|\vec{r}_0;\omega)\, dV_0 + \alpha \oint_{S_0} [G(\vec{r}|\vec{r}_0';\omega)\nabla_0 T(\vec{r}_0';\omega) - T(\vec{r}_0',\omega)\nabla_0 G(\vec{r}|\vec{r}_0';\omega)] \cdot d\vec{S}_0, \tag{2}$$

where S_0 is the surface surrounding the domain volume V_0, which includes the harmonic source $Q(\vec{r}_0,\omega)$; $\vec{r}_0'$ is the source coordinate point on surface S_0, $d\vec{S}_0$ indicates an infinitesimal area vector along the outward direction normal to the boundary surface S_0: $d\vec{S}_0 = \vec{n} dS_0$ with $\vec{n}$ being the outward unit vector. $G(\vec{r}|\vec{r}_0;\omega)$ is the thermal-wave Green function. The adiabatic second-kind (Neumann) boundary condition, representing a heat flux source at the external surface can be applied. The homogeneous boundary conditions for the appropriate Green function and inhomogeneous boundary conditions for the temperature field, respectively, can be written as

$$k\vec{n} \cdot \nabla G(\vec{r}|\vec{r}_0,\omega)|_{r=R_0} = 0, \tag{3}$$

$$k\vec{n} \cdot \nabla T(\vec{r}|\vec{r}_0,\omega)|_{r=R_0} = F(\vec{r}|\vec{r}_0,\omega)|_{r=R_0}, \tag{4}$$

where F is the heat flux ($W\,m^{-2}$) impinging on the cylindrical surface. Therefore, in the absence of volume thermal sources $Q(\vec{r}_0,\omega)$ inside the cylinder, and with the homogeneous boundary conditions for the Green function shown in Eq. (3), the thermal-wave field represented by Eq. (2) can be reduced to

$$T(\vec{r},\omega) = -\left(\frac{\alpha}{k}\right) \oint_S F(\vec{r}_0,\omega) G(\vec{r}|\vec{r}_0;\omega)\, dS_0. \tag{5}$$

Assuming that the incident light flux on the surface is uniform, in conformity with our experimental system, the thermal flux should be weighed by a projection factor [as seen in Fig. 1(b)] in the form of the cosine of the incident uniform intensity and can be expressed as

$$F(R_0, \varphi, \omega) = F_0 \begin{Bmatrix} \cos(\pi/2 - \varphi); & (\pi - \theta_0)/2 \le \varphi \le (\pi + \theta_0)/2 \\ 0; & \text{all other angles.} \end{Bmatrix} \tag{6}$$

The appropriate Green function for the calculation of Eq. (5) can be given with the observation coordinate, r, as the running variable in the form[20,30]

$$G(r, \varphi | r_0, \varphi_0; \omega) = \frac{1}{2\pi\alpha} \sum_{m=-\infty}^{\infty} \frac{e^{im(\varphi-\varphi_0)}}{I'_m(\sigma R_0)} \times \begin{Bmatrix} [I'_m(\sigma R_0)K_m(\sigma r_0) - I_m(\sigma r_0)K'_m(\sigma R_0)]I_m(\sigma r), & 0 \le r \le r_0, \\ [I'_m(\sigma R_0)K_m(\sigma r) - I_m(\sigma r)K'_m(\sigma R_0)]I_m(\sigma r_0), & r_0 \le r \le R_0. \end{Bmatrix} \tag{7}$$

where $I_m(z)$, $K_m(z)$ and $I'_m(z)$, $K'_m(z)$ are the complex-argument modified Bessel functions of the first kind and of the second kind of order m and their derivatives, respectively. Substituting the Green function into Eq. (5) and interchanging $(r, \varphi) \Leftrightarrow (r_0, \varphi_0)$, Eq. (7), so as to allow integrations over the source coordinates (r_0, φ_0), the final thermal-wave field can be expressed as

$$T(r, \varphi, \omega) = \frac{F_0}{2\pi k} \left\{ \frac{2I_0(\sigma r)}{I'_0(\sigma R_0)} \sin\frac{\theta_0}{2} + \frac{I_1(\sigma r)}{I'_1(\sigma R_0)} (\theta_0 + \sin\theta_0) \times \cos\left(\frac{\pi}{2} - \varphi\right) \right.$$
$$\left. + 2\sum_{m=2}^{\infty} \frac{I_m(\sigma r)}{I'_m(\sigma R_0)} \times \cos\left[\frac{m}{2}(\pi - 2\varphi)\right] \left[\frac{\sin\left[\frac{(m+1)\theta_0}{2}\right]}{m+1} + \frac{\sin\left[\frac{(m-1)\theta_0}{2}\right]}{m-1} \right] \right\}. \tag{8}$$

As shown in Eq. (8), if $\theta_0 = 0$, i.e., no light is incident on the surface, the thermal-wave field $T(\vec{r}, \omega) = 0$, as expected. From the structure of this expression it is seen that the thermal-wave field of cylindrical solids under uniform illumination is a strong function of modulation frequency, material thermal diffusivity, and geometric factors, such as the diameter of the cylinder and the detection angle φ.

III. NUMERICAL SIMULATIONS

Based on the analytical formalism above, the thermal-wave-field distribution of a cylindrical solid can be calculated for different parameters. The amplitude and phase of the temperature oscillation on the curved cylindrical surface can be obtained by analyzing the complex signal given in Eq. (8). Considering the fact that the infrared radiation is actually emitted from the surface of the solid and the LIT measurement data are also obtained from the surface, the simulations were restricted to the sample surface at $r = R_0$. The illuminating collimated beam size was assumed to be large enough so as to cover the entire upper part of the cylinder, therefore, $\theta_0 = \pi$ is assumed in the calculation. The other parameters used in the simulation were $F_0 = 1\ \text{W/cm}^2$, $\alpha = 3.95 \times 10^{-6}\ \text{m}^2/\text{s}$, and $k = 16.3\ \text{W/K m}$[34] for AISI 304 stainless steels, where α and k are the thermal diffusivity and the thermal conductivity of the material, respectively. In all simulations, the amplitude and the phase of the surface thermal-wave were normalized to the corresponding amplitude and phase of a flat surface of a semi-infinitely thick sample of the same material in order to enhance the effects of the curved surface. The normalization was performed by amplitude division and phase subtraction of the curved surface and the flat surface of the same material, respectively. The amplitude and the phase on the surface of a semi-infinite flat sample can be calculated from the well-known 1D theoretical model,[30]

$$T(0, \omega) = F_0 \left(\frac{\sqrt{\alpha}}{k\sqrt{\omega}} \right) e^{-i\frac{\pi}{4}}. \tag{9}$$

The thermal-wave field in Eq. (9) clearly exhibits the dependence of the amplitude on frequency and on the constant π/4 phase lag with respect to the incident thermal flux.

Figure 2 shows the normalized amplitude and phase distribution on the curved surface at a fixed cross section of materials with various thermal diffusivities, while other thermophysical properties are assumed to be the same as those of the AISI 304 stainless steel. The radius of the cylinder was $R_0 = 1.5$ mm and the modulation frequency was fixed at 1.0 Hz. The parameters of the flat material used for normalization were also fixed at those of AISI 304 stainless steel for all the different cylinders assumed in Fig. 2. It is seen that both the normalized amplitude and phase from the curved surface are sensitive to the measurement position, angle φ: Even if the thermal parameters of the cylinder and the flat solid are exactly the same, the thermal wave field of the cylinder is totally different. This can be clearly seen in both Figs. 2(a) and 2(b): The normalized amplitude and phase are not equal to 1 and 0, respectively, even at $\varphi = 90°$ where the laser beam is incident normal to the surface. Although a uniform illumination is assumed, the thermal flux is not uniform due to the projectional nature of the incident flux, $k\vec{n} \cdot \nabla T(\vec{r}|\vec{r}_0, \omega)|_{r=R_0}$ on the curved surface. As a result, the

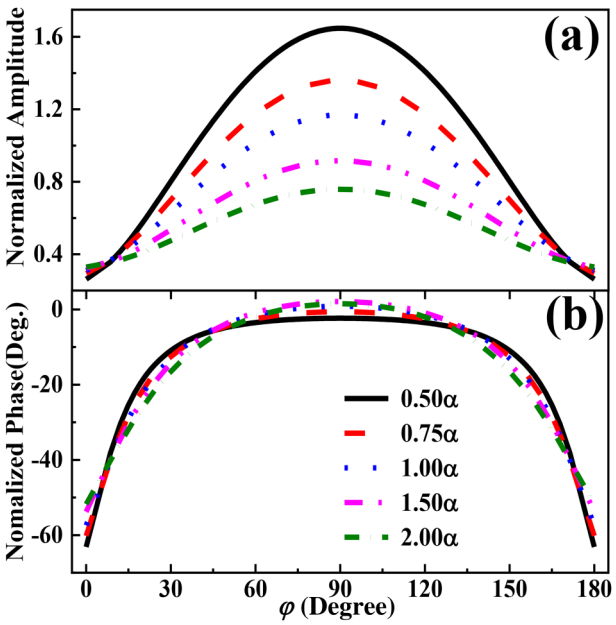

FIG. 2. Effect of thermal diffusivity on the distribution of the normalized amplitude (a) and phase (b) on the curved surface of a cylindrical solid with $R_0 = 1.5$ mm at 1 Hz.

thermal-wave distribution on the sample surface over the angular coordinates becomes bell shaped with a peak value at $\varphi = 90°$, as expected. As the thermal diffusivity increases, the amplitude decreases because the solid becomes a better diffuser with increasing α and the thermal wave spreads deeper into the bulk and also wider laterally along the surface, and the phase lag oscillates at different frequencies, especially at lower frequencies than 100 Hz due to thermal wave interference occurred inside the curved surface. Figure 3 shows the frequency dependence of the normalized amplitude and phase measured at $\varphi = 90°$ with other parameters remaining the same as those in Fig. 2. Here, peaks and valleys can be clearly seen in both amplitude and phase channels, especially in the low frequency range from 0.1 Hz up to 100 Hz, which is most frequently used with LIT imaging. As expected, when the frequency is higher than 1000 Hz, the thermal-wave field of the curved surface tends to that of the flat surface (amplitude ratio with the flat solid ~ a constant (~1 in the case of 1.00α, blue line) and phase difference ~0) owing to the very small thermal diffusion length (defined by $\mu = (2\alpha/\omega)^{1/2}$) compared with the radius of curvature of the cylinder. It is also noted in Fig. 3(b) that the phase exhibits a peak that shifts to a higher frequency with increasing thermal diffusivity, and so does the amplitude. Constructive thermal-wave interference with thermal power confinement along the curved boundary is the source of these signal extrema.

Figure 4 shows the distribution of the normalized amplitude and phase on the curved surface of a cylindrical sample with $R_0 = 1.5$ mm. The material is the same as that in Figs. 2 and 3. The normalized thermal-wave amplitude decreases monotonically toward the edge of the illuminated surface with increased

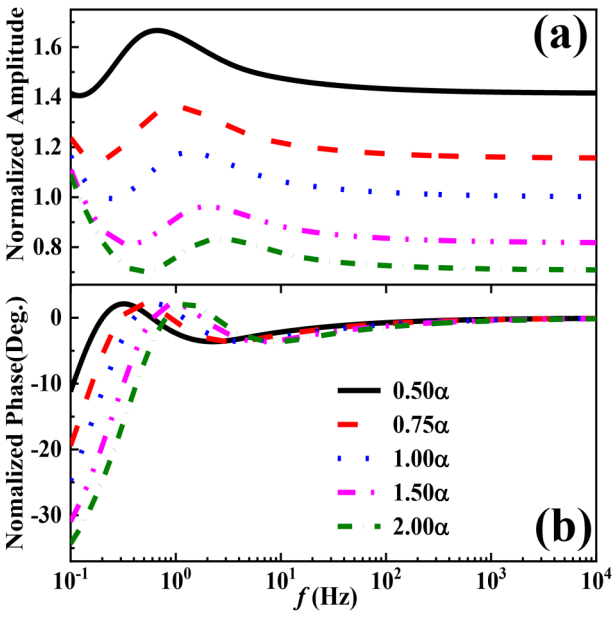

FIG. 3. Modulation frequency dependence of normalized thermal-wave amplitude (a) and phase (b) of the curved surface of a cylinder with $R_0 = 1.5$ mm measured at $\varphi = 90°$ and $\theta_0 = 180°$.

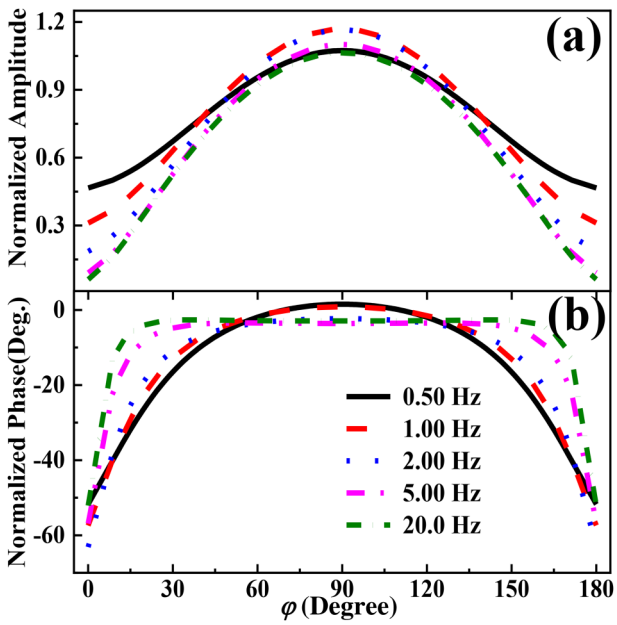

FIG. 4. Normalized amplitude (a) and phase (b) on the curved surface of a cylindrical solid with $R_0 = 1.5$ mm at various modulation frequencies.

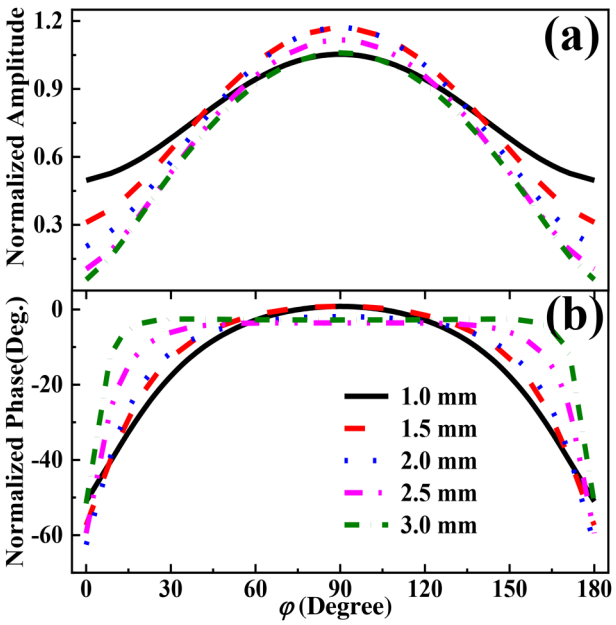

FIG. 5. Normalized amplitude (a) and phase (b) on the curved surface of cylindrical solids with different radii (R_0) at 1.0 Hz modulation frequency.

modulation frequency because the projected thermal flux also decreases. As the frequency increases, the phase becomes flatter over a wider range of the surface. This is as expected owing to the smaller thermal diffusion length at higher frequencies compared with the fixed radius of the cylinder, which results in a thermal wave field that is closer to that of a flat surface.

Figure 5 shows the normalized thermal-wave amplitude and phase response from the curved surfaces of several cylindrical samples with different radii (R_0) at 1.0 Hz modulation frequency. The effect of the diameter of the cylindrical solid on the thermal-wave field is essentially the same as that of the frequency variation shown in Fig. 4. This is as expected because the effect of the surface curvature on the thermal-wave field depends primarily on the relative value of the thermal diffusion length and the radius of curvature of the solid surface. The thermal diffusion length decreases when frequency increases, which is equivalent to the effect of increasing the radius of curvature at a fixed frequency, as shown in comparing Figs. 4 and 5. For the same reason, when the radius of the cylinder is increased, the phase becomes flatter as the curvature tends toward the flat solid limit.

In LIT imaging measurements of cylindrically curved solids, different detection schemes in terms of the relative orientation between the incident illumination and the thermal image (usually infrared cameras) may be employed. Figure 6 shows the orientation relation between the incident illumination and the thermal camera. Here, the illumination is assumed to be incident vertically onto the surface (i.e., $\varphi = 90°$) and the collimated illumination beam covers the entire top-half surface of the cylinder. The angle between the illumination and the imager is denoted as Δ. Considering the

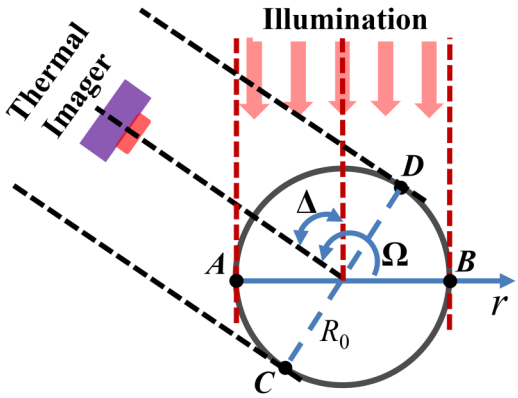

FIG. 6. Schematic of the relative orientation between incident illumination and thermal imaging direction.

Lambert cosine law, the thermal radiation intensity from the curved cylindrical surface that is received by the thermal imager must be theoretically revised as follows:

$$I_{imager} = T(R_o, \varphi, \omega)\cos(\vartheta - \Omega), \quad \left(\Omega - \frac{\pi}{2}\right) \le \vartheta \le \left(\Omega + \frac{\pi}{2}\right), \tag{10}$$

where $T(R_o, \varphi, \omega)$ is the thermal-wave field calculated from Eq. (8) and Ω represents the directional angle of the imager in the same coordinates as the cylindrical system in Fig. 1. Figure 7 shows the simulated LIT signal (amplitude and phase) at various orientations of the infrared camera after taking the Lambertian distribution of the emitted infrared radiation into account. A cylindrical sample of AISI 304 stainless steel with a radius of 1 mm at 2 Hz was assumed in the simulation. It is seen from Fig. 7 that the amplitude and phase of the LIT signal exhibit different behavior when the camera is placed at different positions, while the illumination direction is fixed. The values in the LIT amplitude channel are different from those of the thermal-wave field alone because they are weighed by the Lambert cosine factor used in the projection of the local infrared radiation at normal direction to the camera. When the camera is placed at any other position, both the amplitude and phase change due to the angular divergence between the illuminated and detected areas, i.e., illuminating the curved surface from A to B but detecting the thermal-wave field in the region from C to D as shown in Fig. 6. Nevertheless, the different LIT signal responses allow the optimization of the experimental arrangement and detection sensitivity.

IV. EXPERIMENTAL RESULTS AND DISCUSSION

To explore the LIT capability for quantitative imaging of curved cylindrical solids, experiments were performed using a series of AISI 304 cylindrical steel samples with different diameters. The experimental setup for LIT imaging is shown in Fig. 8. A semiconductor laser diode (~40 W, 808 nm) was used as the optical excitation source of thermal waves. The laser beam was expanded

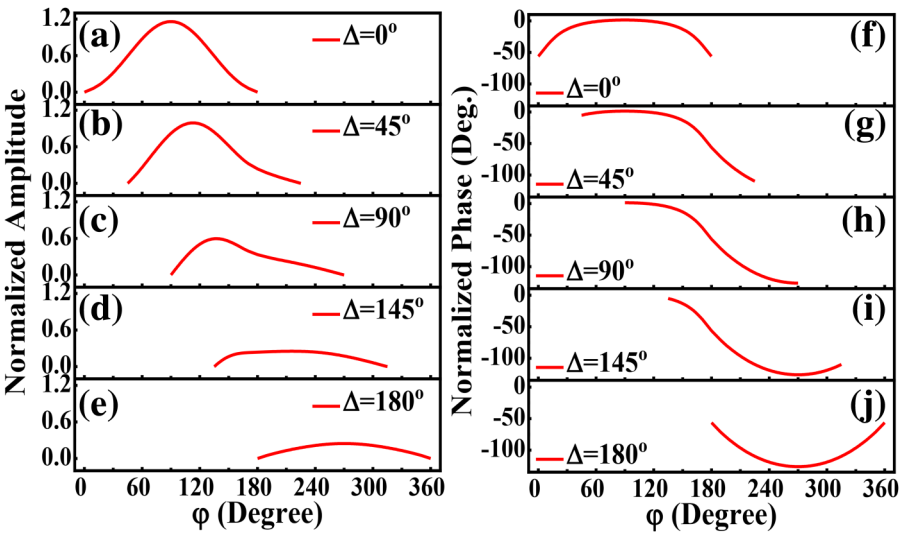

FIG. 7. Simulated LIT amplitude [(a), (b), (c), (d), and (e)] and phase [(f), (g), (h), (i), and (j)] considering the Lambertian distribution of infrared radiation at various orientations of the infrared camera.

and collimated onto the curved surface of the sample with a spot size of ~40 mm so as to be large enough to cover the whole projected sample surface, i.e., $\theta_0 = \pi$ in Fig. 1 in all experiments. The laser output was modulated by a periodic current driver, and the modulation frequency (which also served as the lock-in reference), was controlled by a computer with Labview software. The harmonically modulated infrared radiation emitted from the sample surface was detected by a mid-infrared camera (NoxCam 640BB, pixel size 15 μm). The camera signals were collected by the computer and a digital lock-in algorithm was used to process the signal data and demodulate pixel signals in the form of amplitude and phase images. The digital lock-in algorithm used in the experiment is implemented as follows: A time sequential images from the camera are first collected and the data in the images are written in the format of 3-dimensional matrix of 640*512*N, where 640*512 is the pixels of the camera and N is the number of the images that are taken. For each pixel, the LIT amplitude and phase can be calculated in that the time sequential signals of the pixel is multiplied by the reference signals with either 0 or 90° phase delay of the same frequency and then integrated numerically. The LIT amplitude and phase images can thus be calculated in parallel by the two integration results (S_0 from 0 degree phase delay or S_{90} from 90° phase delay) for each pixel with amplitude $A = \sqrt{S_0^2 + S_{90}^2}$ and phase $P = \arctan(S_{90}/S_0)$. All the experiments were carried out at room temperature of ~300 K.

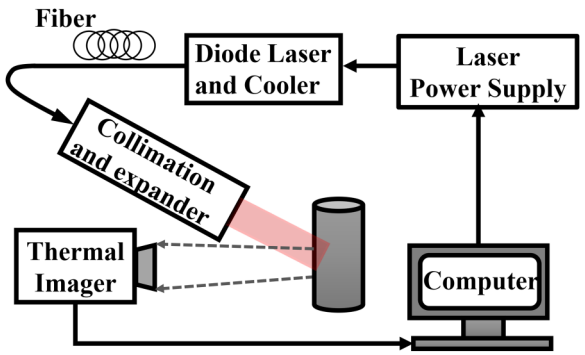

FIG. 8. Configuration of the LIT experimental setup.

The experiment was first performed on an AISI 304 cylindrical steel sample with a 1-mm radius and modulation frequencies 0.5 Hz and 2 Hz. The infrared camera was placed at an angle of ~17° with respect to the illumination direction, i.e., $\Delta \sim 17°$ in Fig. 6. Figure 9 shows the experimental LIT images and corresponding line scans at a typical height of the cylinder, e.g., pixel row No. 290. The black solid lines in the line scan, i.e., Figs. 9(c), 9(d), 9(g), and 9(h) represent the theoretical best fits based on the Lambert cosine law as described by Eq. (10). It is seen from Fig. 9 that the experimental phase is in very good agreement with the theory, while the experimental amplitude data deviate from the theoretical response. The large deviation shown in the phase channel, Figs. 9(d) and 9(h), at both edges of the cylinder (very last 1 or 2 points) is due to detection at the extreme boundary between curved surface of steel solid and air: The last 1 or 2 camera pixels responsible for imaging the boundary area generate a very weak signal-to-noise ratio (SNR) owing to the near-vertical orientation of the curved surface with respect to the illuminating optical flux. This results in weak amplitude and phase responses at the air/steel boundary which may also include possible contributions from surface machining and roughness-layer-induced poorer thermal conductivity and diffusivity.

The major physical mechanism behind the deviation between the theoretical best fits and the experiment was investigated farther. It was found that the deviation between the experimental data and the theory, mainly in the amplitude channel, was due to using the Lambert cosine law usually invoked in ideal theoretical cases. With practical infrared detection systems, experimental factors in addition to the ideal Lambertian cosine law must be considered. Equation (11) shows the possible factors that may be coupled into

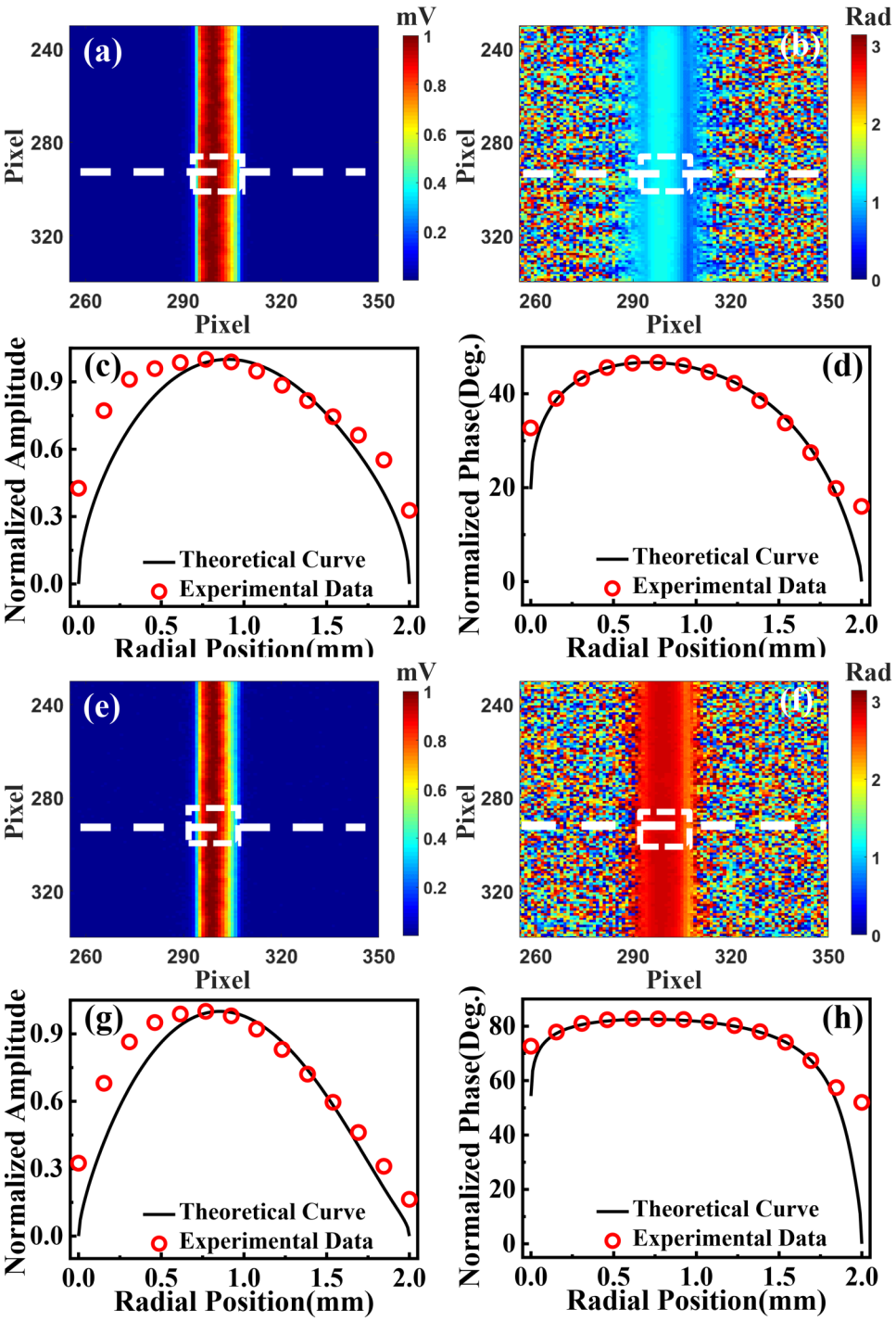

FIG. 9. Experimental LIT images of an AISI 304 steel cylinder with a radius of 1 mm at two frequencies and the corresponding line scans at a typical height of the cylinder. (a) amplitude at 0.5 Hz; (b) phase at 0.5 Hz; (c) line scan of amplitude at pixel row No. 290 at 0.5 Hz; (d) line scan of phase at pixel row No. 290 at 0.5 Hz; (e) amplitude at 2 Hz; (f) phase at 2 Hz; (g) line scan of amplitude at pixel row No. 290 at 2 Hz; and (h) line scan of phase at pixel row No. 290 at 2 Hz.

the pixel response of the infrared camera,

$$I(r, \varphi, \omega) = T(r, \varphi, \omega)\varepsilon(\varphi, \omega)H_1(\varphi, \omega), \quad (11)$$

where I is the detected signal by the camera, T is the thermal-wave field of the cylindrical sample, $\varepsilon(\varphi, \omega)$ is an angular factor related not only to the Lambertian behavior, but also to sample shape and surface condition, including roughness and non-uniformity of the

surface that may measurably affect the angularly dependent emissivity and thus the detected LIT images. H_1 is the response function of the imaging system including both optical and electronic factors. In practice, these factors, i.e., the product of $\varepsilon(\varphi, \omega)H_1(\varphi, \omega)$, are difficult to measure individually, but can be lumped together as an instrumental-response-integrated factor. Figure 10 shows an infrared image of the surface of the same cylindrical steel and at the same experimental orientation as that in Fig. 9 right after the sample was illuminated by the laser and heated up to ~25 °C higher than the room temperature. The image was obtained after blocking the laser beam so as to avoid any possible interference with the mid-IR response of the sample surface. This infrared image contains all instrumental and Lambertian information from the curved sample surface, including surface shape and finish and both optical and electronic instrumental response function described in Eq. (11). The image Fig. 10(a) can be employed as an empirical angular distribution function to replace the ideal Lambert cosine function assumed in the theoretical model. Figure 10(b) shows a line scan of the infrared image of Fig. 10(a) at pixel row 290. It is seen that the distribution of detected infrared intensity on the focal plane array (FPA) detector is very different from that of the ideal cosine function. A fitted polynomial function [solid line in Fig. 10(b)] can be employed as an empirical radiation emission distribution function to normalize the obtained images for quantitative purposes. Figures 10(c)–10(f) show a comparison between the experimental results (exactly the same as those in Fig. 9) and the modified theoretical results using the thus derived empirical distribution function. It is seen that the normalized theoretical results are now in excellent agreement with the pixel-row data obtained at both 0.5 Hz and 2 Hz.

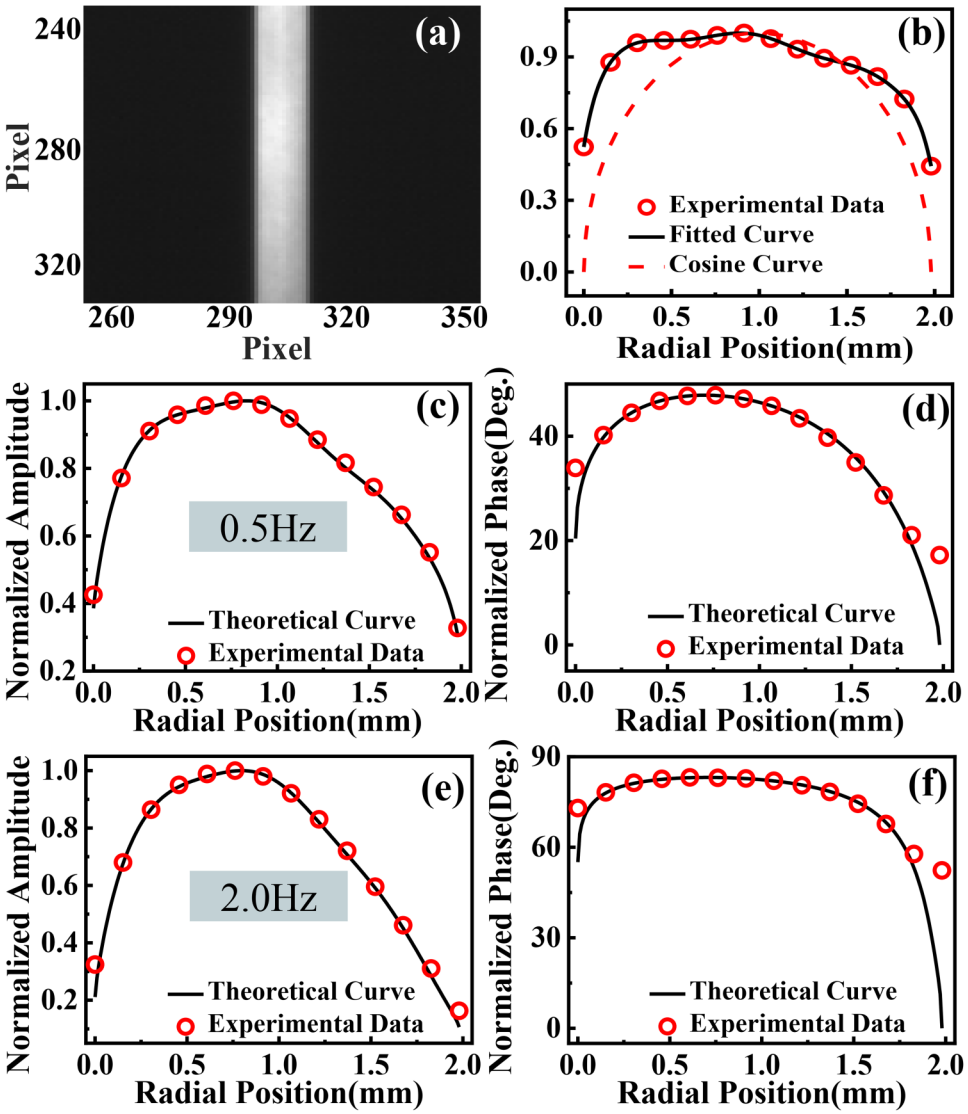

FIG. 10. (a) Background infrared image without laser illumination; (b) line scan of the intensity in (a) at pixel row No. 290; (c) LIT amplitude and (d) LIT phase at 0.5 Hz; (e) LIT amplitude; and (f) LIT phase of the cylinder with a 1-mm radius at 2 Hz.

The large radial position (beyond 1.7 mm) discrepancy remains, however, as material inhomogeneity and extreme-boundary-region poor SNR cannot be accounted for by the foregoing normalization procedures.

Figure 11 shows amplitude and phase LIT images and corresponding line scans at pixel row 290 of an AISI steel cylinder of 2-mm radius at $f = 0.5$ Hz, 2 Hz, and 5 Hz. During the experiment, the relative orientation among the camera, illuminating laser and sample remained unchanged at all frequencies. The relative angle

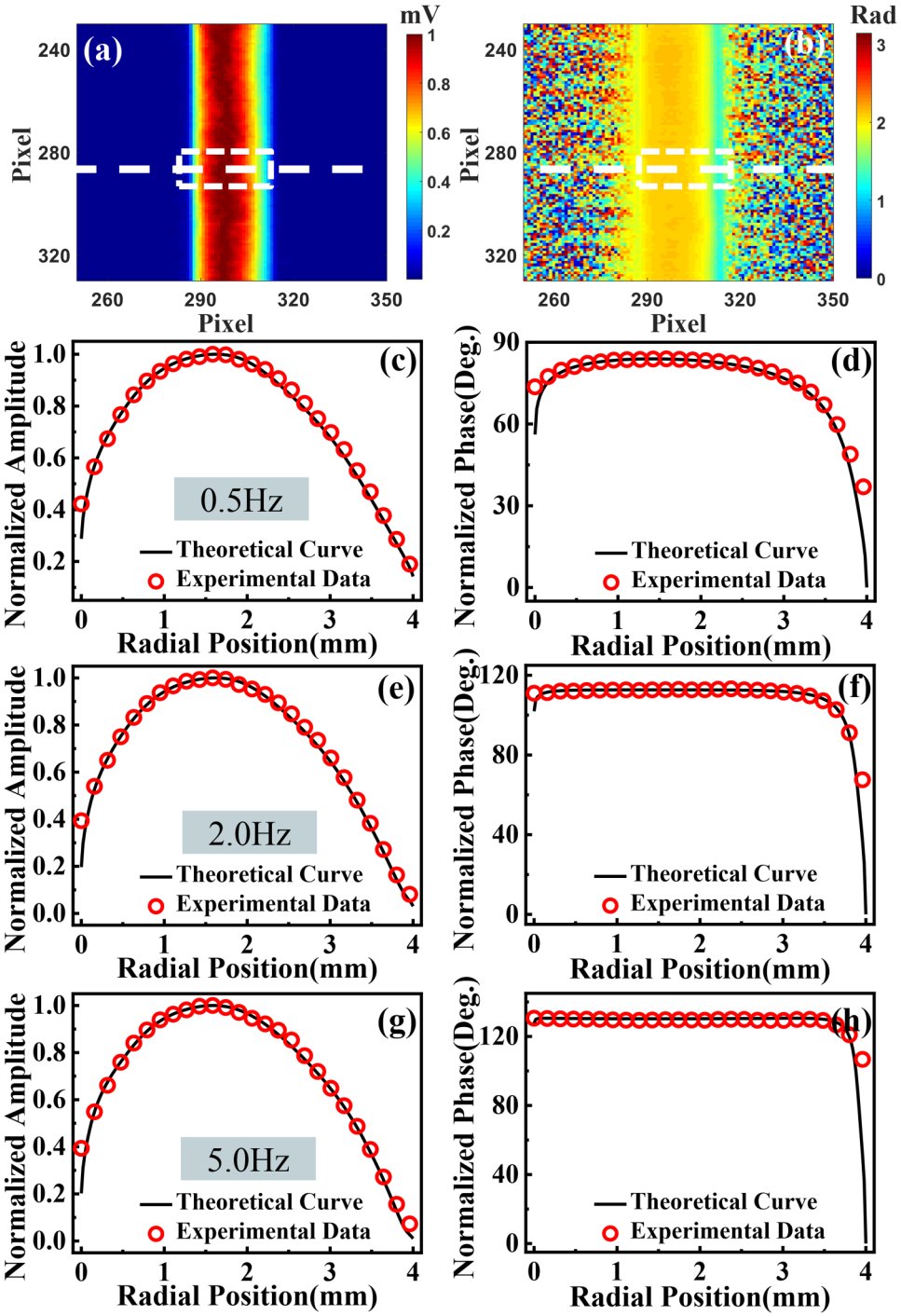

FIG. 11. LIT images (a) amplitude and (b) phase at 0.5 Hz; and pixel line scan amplitude [(c),(e), and (g)] and phase [(d), (f), and (h)] of the cylinder with a radius of 2 mm at 0.5 Hz, 2 Hz, and 5 Hz, respectively.

(Δ) between the laser illumination direction and the camera was around ~17° as mentioned earlier. Theoretical best fitting was performed with a MATLAB program, in which the empirical angular distribution function was measured and used. During the best-fitting process, the thermal diffusivity (α) and the orientation angle (Δ) were set as fitted parameters. It is seen that both the experimental amplitude and phase best fits to the theory are excellent. Their values (α, Δ) are: (3.74×10^{-6} m^2/s, 16.86°), (3.76×10^{-6} m^2/s,

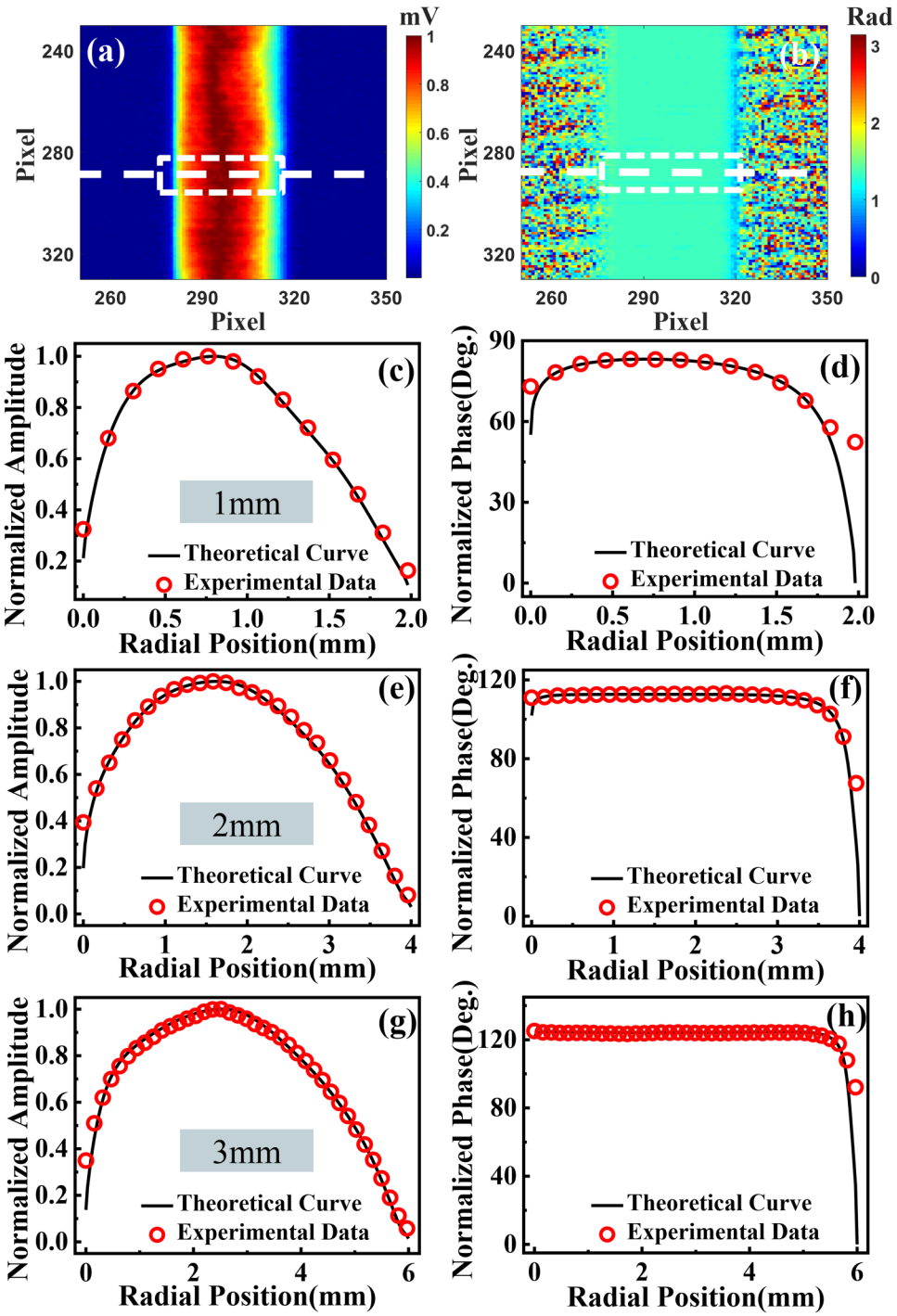

FIG. 12. LIT (a) amplitude and (b) phase images of cylinders of 3-mm radius; and pixel line scans of amplitude [(c),(e), and (g)] and phase [(d), (f), and (h)] of cylinder with radii 1 mm, 2 mm, and 3 mm, respectively at 2 Hz.

16.55°), and (3.77×10^{-6} m^2/s, 16.60°) at 0.5 Hz, 2 Hz, and 5 Hz, respectively. The thus obtained thermal diffusivities are consistent across all three frequencies, and the orientation angle (Δ) is also consistent with ~17° set in the experiment. The mean thermal diffusivity averaged over the measurements at all three frequencies is 3.76×10^{-6} m^2/s, which is also consistent with the literature value[34] within ~5.29%: For AISI304 steel, the reported thermal diffusivity is 3.95×10^{-6} m^2/s at 300 K and 4.08×10^{-6} m^2/s at 400 K. Considering the fact that the actual temperature of the laser irradiated cylinder rose to the steady value of ~315 K during the experiment, the

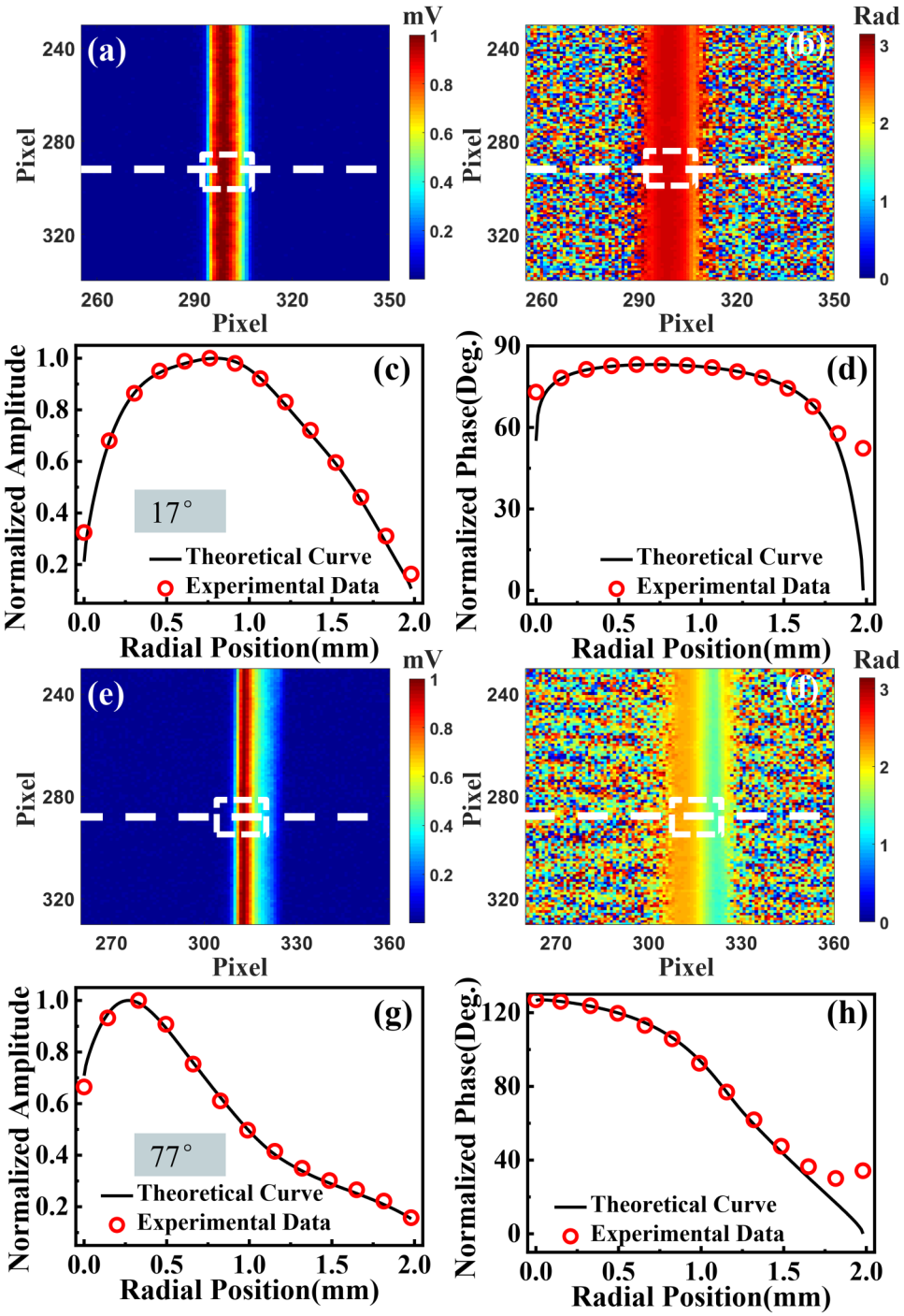

FIG. 13. LIT images and the corresponding line scans with different orientation angles for the radius of 1 mm sample at 2 Hz. (a) and (c) LIT amplitude image and its line scan at Δ = 17°; (b) and (d) LIT phase image and its line scan at Δ = 17°; (e) and (g) LIT amplitude image and its line scan at Δ = 77°; (f) and (h) LIT phase image and its line scan at Δ = 77°.

theoretical thermal diffusivity of the sample at 315 K is calculated to be about 3.97×10^{-6} m^2/s if a linear interpolation is assumed.

Figure 12 shows amplitude and phase LIT images and line scans at pixel row 290 of the AISI 304 steel cylindrical samples with different radii (1 mm, 2 mm, and 3 mm) at 2 Hz. The relative orientations among the camera, illuminating laser and sample center axis remained fixed for all samples during the experiments. The empirical angular distribution function for all samples was measured before LIT imaging and was used in the theoretical best fits. Again, the thermal diffusivity (α) and orientation angle (Δ) were set as the fitting parameters. It is seen from Fig. 12 that both experimental amplitude and phase fits to the theory are excellent. The best fitted (α, Δ) results were: (3.78×10^{-6} m^2/s, 16.78°), (3.76×10^{-6} m^2/s, 16.55°), and (3.91×10^{-6} m^2/s, 16.36°) for the samples with radius of 1 mm, 2 mm, and 3 mm, respectively. The best-fitted thermal diffusivities are self-consistent and the orientation angle (Δ) is also consistent with that set (~17°) in the experiment. Compared with the interpolated literature value of the thermal diffusivity at 315 K (3.97×10^{-6} m^2/s), the relative errors of the best-fitted value were ~4.79%, 5.59%, and 1.51%, respectively, for the samples of radius 1 mm, 2 mm, and 3 mm. It should be noted that there are some non-uniformity shown in LIT images at different rows in Fig. 11 and Fig. 12. Detailed examinations on the normalized line-scan of the LIT amplitude and phase images at different rows show that all the normalized line-scans of amplitude and phase are well overlapped and are well consistent each other, which means the seemingly non-uniformity in LIT images will have very limited effect on the determination of thermophysical parameters.

Finally, the effect of the orientation angle (Δ) between the illuminating beam direction and the camera on the cylindrical sample LIT images was examined. In the experiment, the direction of illumination was fixed while the direction of the camera was varied. Figure 13 shows LIT images and the corresponding line scans at two orientation angles (approximately $\Delta \sim 17°$ and ~77°) for the 1-mm radius sample at 2 Hz. Again, the empirical angular distribution function at the two orientation angles was measured before LIT imaging and then was used in the theoretical best fits. It is seen that amplitudes and phases at both orientations were well fitted to the theoretical values with the notable exception of the phases at radial positions beyond 1.7 mm. The best-fit values of thermal diffusivity and orientation angle (α, Δ) were: (3.78×10^{-6} m^2/s, 16.78°) and (3.82×10^{-6} m^2/s, $\Delta = 76.41°$) for the two orientations, respectively. These pairs of values are highly consistent with the literature and also the orientations set in the experiments. The poor phase agreement at large radial positions is once again attributed to the same extreme boundary poor SNR and thermophysical property variations in the nearly tangentially probed surface boundary layer created by the tool machining of the steel cylinders, resulting in inhomogeneous surface layers.

V. CONCLUSIONS

In summary, we extended the applications of the LIT technique from flat surfaces to quantitative imaging of solids with continuously curved cylindrical surfaces, in which both the photothermally induced surface temperature and the angularly dependent infrared radiation emission from the curved surface varied over the entire angular distribution. A theoretical photothermal model was established based on the Green function method from which the thermal-wave field distribution at various azimuthal angles on the curved surface was obtained. Physical characteristics of the thermal-wave field interaction with the collimated heating laser beam and different material and measurement parameters were discussed. Quantitative LIT imaging experiments were conducted on AISI 304 cylindrical steel samples with different diameters and measurement configurations. It was found that the angularly dependent infrared radiation of the curved surfaces could be precisely obtained with an empirical infrared image normalization obtained from the same sample. The experimental results were in excellent agreement with the theory, thereby rendering the developed imaging technique into an important practical methodology for quantitative non-destructive and non-contacting LIT imaging of thermophysical and geometrical properties of any curved solid surfaces.

ACKNOWLEDGMENTS

This work was supported by a grant from the National Natural Science Foundation of China (Contract No. 60877063), Scientific Research Foundation for Returned Scholars, Ministry of Education of China, and the project of the Priority Academic Program Development (PAPD) of Jiangsu Higher Education Institutions. The Canada Research Chairs and the Natural Sciences and Engineering Research Council of Canada are gratefully acknowledged for their support through a CRC Tier I award and a Discovery Grant, respectively, to A.M.

DATA AVAILABILITY

The data that support the findings of this study are available from the corresponding author upon reasonable request.

REFERENCES

[1]P.-E. Nordal and S. Kanstad, "Photothermal radiometry," Phys. Scr. **20**, 659 (1979).
[2]P.-E. Nordal and S. Kanstad, "Visible-light spectroscopy by photothermal radiometry using an incoherent source," Appl. Phys. Lett. **38**, 486 (1981).
[3]P.-E. Nordal and S. O. Kanstad, "New developments in photothermal radiometry," Infrared Phys. **25**, 295 (1985).
[4]A. Mandelis, "Laser infrared photothermal radiometry of semiconductors: Principles and applications to solid state electronics," Solid State Electron. **42**, 1 (1998).
[5]T. T. N. Lan, U. Seidel, and H. G. Walther, "Theory of microstructural depth profiling by photothermal measurements," J. Appl. Phys. **77**(9), 4739 (1995).
[6]H. Qu, C. Wang, X. Guo, and A. Mandelis, "Reconstruction of depth profiles of thermal conductivity of case hardened steels using a three-dimensional photothermal technique," J. Appl. Phys. **104**, 113518 (2008).
[7]I. A. Vitkin, "Biophysical studies of pulsed photothermal radiometry in tissues and tissuelike media," Med. Phys. **24**(12), 2056 (1997).
[8]W. P. Leung and A. C. Tam, "Thermal conduction at a contact interface measured by pulsed photothermal radiometry," J. Appl. Phys. **63**(9), 4505 (1988).
[9]L. Nicolaides, C. Feng, A. Mandelis, and S. H. Abrams, "Dental dynamic diagnostics using simultaneous frequency-domain PTR and laser luminescence," Anal. Sci. **17**, S330 (2001).
[10]C. Wang and A. Mandelis, "Case depth determination in heat-treated industrial steel products using photothermal radiometric interferometric phase minima," NDT E Int. **40**(2), 158 (2007).

[11]I. Kaufman, P.-T. Chang, H.-S. Hsu *et al.*, "Photothermal radiometric detection and imaging of surface cracks," J. Nondestruct. Eval. **6**(2), 87 (1987).
[12]J.-Y. Liu, A. Melnikov, and A. Mandelis, "Silicon solar cell electrical parameter measurements through quantitative lock-in carrierographic (photoluminescence) and thermographic imaging," Phys. State Solidi A **210**(10), 2135 (2013).
[13]G. Busse, D. Wu, and W. Karpen, "Thermal wave imaging with phase sensitive modulated thermography," J. Appl. Phys. **71**, 3962 (1992).
[14]D. Wu and G. Busse, "Lock-in thermography for nondestructive evaluation of materials," Rev. Gén. Therm. **37**(8), 693 (1998).
[15]S. Huth, O. Breitenstein, A. Huber, and U. Lambert, "Localization of gate oxide integrity defects in silicon metal-oxide-semiconductor structures with lock-in IR thermography," J. Appl. Phys. **88**(7), 4000 (2000).
[16]D. Bates, G. Smith, D. Lu, and J. Hewitt, "Rapid thermal non-destructive testing of aircraft components," Compos. B **31**(3), 175 (2000).
[17]A. Melnikov, A. Mandelis, J. Tolev *et al.*, "Infrared lock-in carrierography (photocarrier radiometric imaging) of Si solar cells," J. Appl. Phys. **107**, 114513 (2010).
[18]Y. Hirayama, R. Iguchi, X. F. Miao, K. Hono, and K. Uchida, "High-throughput direct measurement of magnetocaloric effect based on lock-in thermography technique," Appl. Phys. Lett. **111**(16), 163901 (2017).
[19]H. Nakajima, T. Morimoto, Y. Okigawa, T. Yamada, Y. Ikuta, K. Kawahara, H. Ago, and T. Okazaki, "Imaging of local structures affecting electrical transport properties of large graphene sheets by lock-in thermography," Sci. Adv. **5**(2), eaau3407 (2019).
[20]C. Wang, A. Mandelis, and Y. Liu, "Photothermal radiometry with solid cylindrical samples," J. Appl. Phys. **96**(7), 3756 (2004).
[21]C. Wang, A. Mandelis, and Y. Liu, "Thermal-wave nondestructive evaluation of cylindrical composite structures using frequency-domain photothermal radiometry," J. Appl. Phys. **97**(1), 014911 (2005).
[22]C. Wang and A. Mandelis, "Characterization of hardened cylindrical C1018 steel rods (0.14%–0.2% C, 0.6%–0.9% Mn) using photothermal radiometry," Rev. Sci. Instrum. **78**(5), 054902 (2007).
[23]G. Xie, J. Zhang, L. Liu *et al.*, "Thermal conductivity depth-profile reconstruction of multilayered cylindrical solids using the thermal-wave Green function method," J. Appl. Phys. **109**(11), 113534 (2011).
[24]A. Salazar and R. Celorrio, "Application of the thermal quadrupole method to the propagation of thermal waves in multilayered cylinders," J. Appl. Phys. **100**(11), 113535 (2006).
[25]R. Celorrio, A. Mendioroz, E. Apiñaniz, A. Salazar, C. Wang, and A. Mandelis, "Reconstruction of radial thermal conductivity depth profile in case hardened steel rods," J. Appl. Phys. **105**, 083517 (2009).
[26]C. Wang, A. Mandelis, Y. Liu *et al.*, "Frequency domain photothermal radiometry with spherical solids," J. Appl. Phys. **101**(8), 083503 (2007).
[27]G. Xie, Z. Chen, C. Wang *et al.*, "Laser induced thermal-wave fields in bilayered spherical solids," Rev. Sci. Instrum. **80**(3), 034903 (2009).
[28]J. Zhang, G. Xie, C. Wang, and A. Mandelis, "Laser induced thermal-wave fields in multi-layered spherical solids based on Green function method," J. Appl. Phys. **112**, 033521 (2012).
[29]N. Madariaga and A. Salazar, "Propagation of thermal waves in multilayered spheres," J. Appl. Phys. **101**(10), 103534 (2007).
[30]A. Mandelis, *Diffusion-Wave Fields: Mathematical Methods and Green Functions* (Springer, New York, 2001).
[31]J. V. Beck, K. D. Cole, A. Haji-Sheikh, and B. Litkouhi, *Heat Conduction Using Green's Functions* (Hemisphere Publishing Corporation, Washington, DC, 1992).
[32]R. Tai, J. Zhang, C. Wang, and A. Mandelis, "Thermal-wave fields in solid wedges using the Green function method: Theory and experiment," J. Appl. Phys. **113**(13), 133501 (2013).
[33]M. Wang, A. Mandelis, A. Melnikov, and C. Wang, "Quantitative lock-in thermography imaging of thermal-wave spatial profiles and thermophysical property measurements in solids with inner corner geometries using thermal-wave field theory," J. Appl. Phys. **124**, 205106 (2018).
[34]F. P. Incropera, *Fundamentals of Heat and Mass Transfer*, 3rd ed. (Wiley, New York, 1990).